Volume 6 | Number 7 | 7 April 2014 | Pages 3425–3896

# Nanoscale

www.rsc.org/nanoscale

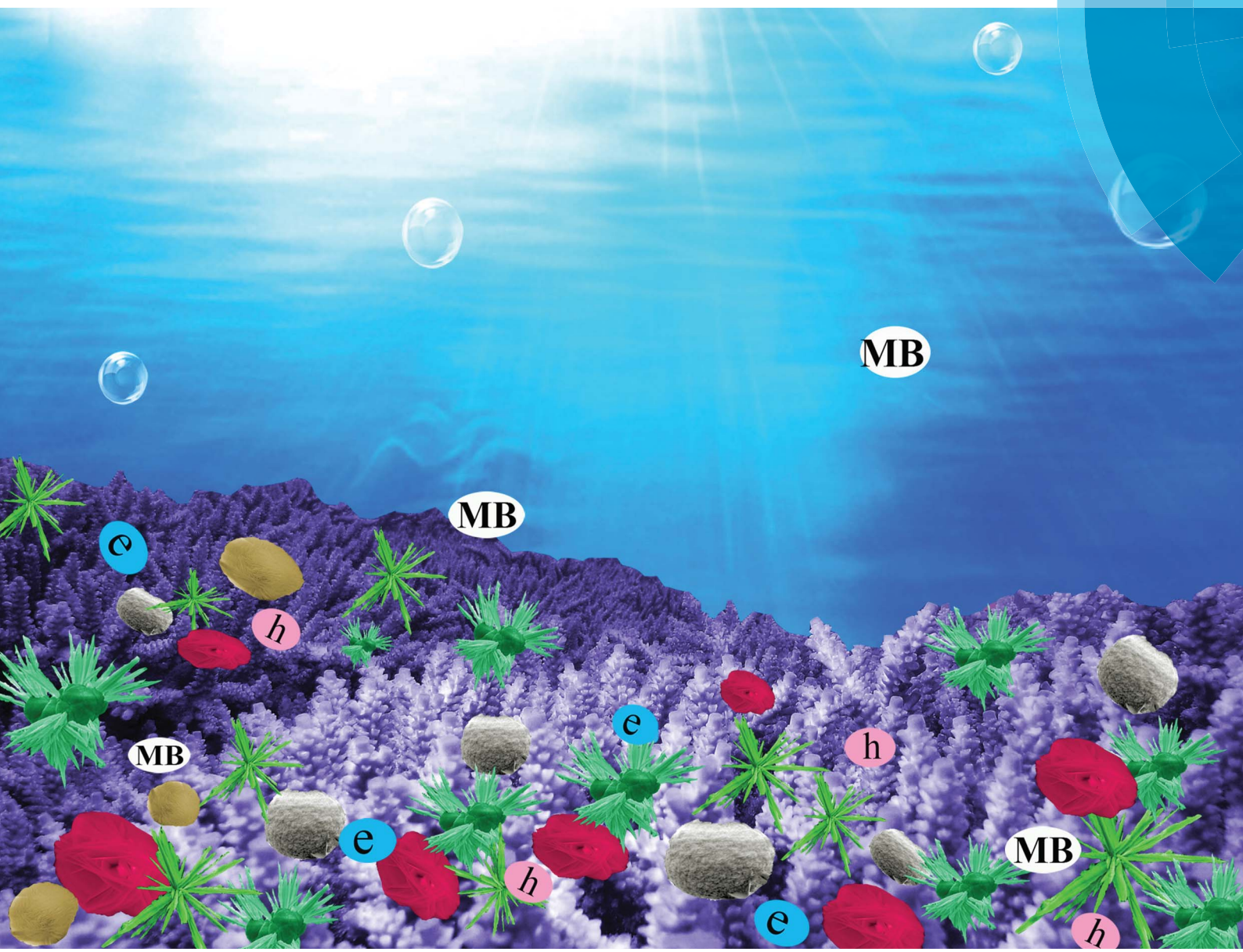


ISSN 2040-3364

ROYAL SOCIETY OF CHEMISTRY

PAPER
Lin, Lin *et al.*
Garden-like perovskite superstructures with enhanced photocatalytic activity

NCNST

Nanoscale

PAPER

View Article Online
View Journal | View Issue

# Garden-like perovskite superstructures with enhanced photocatalytic activity†

Cite this: *Nanoscale*, 2014, **6**, 3576

Meidan Ye,[ab] Mengye Wang,[ab] Dajiang Zheng,[ab] Nan Zhang,[a] Changjian Lin*[a] and Zhiqun Lin*[b]

By subjecting amorphous flower-like $TiO_2$ to a facile hydrothermal synthesis in the presence of $Sr^{2+}$, garden-like perovskite $SrTiO_3$ superstructures were achieved. The amorphous $TiO_2$ was preformed using ZnO flowers as templates. Different three-dimensional $SrTiO_3$ architectures were coexisted in the garden, including $SrTiO_3$ flowers composed of several hollow sword-shaped petals, many sheet-shaped petals or numerous flake-shaped petals, and $SrTiO_3$ grass consisting of a number of long blades. These $SrTiO_3$ superstructures were simultaneously grown on fluorine-doped tin oxide (FTO) substrates. On the basis of a comprehensive study on the effects of growth time, temperature, initial concentrations of precursor, and pH, the formation of these various hierarchical architectures was attributed primarily to the dissolution of amorphous $TiO_2$ and precipitation of perovskite crystals, followed by the Ostwald ripening process of perovskite nanocrystals and self-organization of perovskite building blocks. Interestingly, this approach can be readily extended to create other perovskite structures, including dendritic $BaTiO_3$ and nest-like $CaTiO_3$, as well as $PbTiO_3$ transformed from plate-like pyrochlore $Pb_2Ti_2O_6$ after post-thermal treatment. Garden-like $SrTiO_3$ superstructures showed a superior photocatalytic performance when compared to other as-prepared semiconductors and perovskite materials (*i.e.*, ZnO, $TiO_2$, $BaTiO_3$, $CaTiO_3$ and $PbTiO_3$), probably due to their intrinsic photocatalytic activity and special garden-like features with a coexistence of various structures that significantly facilitated the adsorption and diffusion of methyl blue (MB) molecules and oxygen species in the photochemical reaction of MB degradation.

Received 18th October 2013
Accepted 16th December 2013

DOI: 10.1039/c3nr05564g

www.rsc.org/nanoscale



## 1. Introduction

Perovskite-type oxides $MTiO_3$ (M = Ca, Ba, Sr, Pb, *etc.*) have been extensively studied because of their unique properties for a wide range of applications in catalytic, superconductor, thermoelectric, ferroelectric, piezoelectric, and dielectric devices.[1–3] In particular, perovskite nanostructures have recently received considerable attention due to their enhanced performance as compared to the bulk counterparts.[3–6] Among various $MTiO_3$, such as a typical ternary perovskite-type oxide with large dielectric nonlinearity, temperature-dependent dielectric ability, and low microwave losses, $SrTiO_3$ is a functional material for microwave devices operating at low temperature.[7] Moreover, $SrTiO_3$ is also a cubic-perovskite-type semiconductor with a band gap of approximately 3.2 eV. It has been widely recognized as an effective photocatalyst for water splitting and degradation of organic pollutants owing to its excellent thermal and photo-stabilities, photocatalytic activity, and good structural stability as the framework for metal ion doping.[8–13]

It is noteworthy that the properties of functional materials not only depend strongly on the chemical composition, but also are sensitive to the crystal structure, size and morphology. Therefore, in recent years great efforts have been concentrated on the controllable preparation of materials with versatile structures and tailored properties.[5,6,14–18] The self-organization of nanoscale functional building blocks, including nanosheets,[19–21] nanorods,[5,22,23] nanoparticles,[12,17,24] to form complex hierarchical structures offers great potential for use in energy conversion and storage applications. It is noteworthy that there has been little work on the fabrication of hierarchically structured $SrTiO_3$. For example, dendrite-like $SrTiO_3$ structures were obtained by a hydrothermal process,[22] and mesoporous $SrTiO_3$ spheres composed of nanoparticles[24] and hollow $SrTiO_3$ microspheres constructed by the assembly of nanocubes[12] were produced through modified hydrothermal methods. Clearly, developing a feasible approach to yield diverse hierarchical

[a]*State Key Laboratory of Physical Chemistry of Solid Surfaces and Department of Chemistry, College of Chemistry and Chemical Engineering, Xiamen University, Xiamen 361005, China. E-mail: cjlin@xmu.edu.cn*

[b]*School of Materials Science and Engineering, Georgia Institute of Technology, Atlanta, GA 30332, USA. E-mail: zhiqun.lin@mse.gatech.edu*

† Electronic supplementary information (ESI) available: FESEM images and the XRD pattern of $SrTiO_3$ films (effects of growth temperature, initial precursor concentration, and pH value), EDS analysis of ZnO, $TiO_2$ and $SrTiO_3$, the XRD pattern and PL spectra of $PbTiO_3$, UV-vis spectra of different films, and UV photo-degradation of MB. See DOI: 10.1039/c3nr05564g

structures of $SrTiO_3$ with effective catalytic responses remains challenging.

In this work, a large variety of $SrTiO_3$ hierarchical architectures (*i.e.*, garden-like superstructures) were successfully created by a facile hydrothermal treatment of amorphous flower-like $TiO_2$ preformed using the ZnO flowers as templates. The introduction of ZnO templates was motivated by exploiting an amorphous yet 3D structured $TiO_2$ prototype as the titanium source for the $SrTiO_3$ formation. The time-dependent evolution study revealed that the formation of these diverse hierarchical architectures can be attributed primarily to the dissolution of amorphous $TiO_2$ and precipitation of perovskite crystals, followed by the Ostwald ripening process of perovskite nanocrystals and self-organization of perovskite building blocks. Remarkably, this preparative strategy can be readily extended to produce other hierarchical perovskite materials, including dendrite-shaped $BaTiO_3$ and nest-shaped $CaTiO_3$, as well as pyrochlore $Pb_2Ti_2O_6$ which was further transformed into $PbTiO_3$ by calcination. Quite intriguingly, in comparison to other semiconductors and perovskite materials (*i.e.*, ZnO, $TiO_2$, $BaTiO_3$, $CaTiO_3$ and $PbTiO_3$), garden-like $SrTiO_3$ superstructures exhibited a superior photocatalytic performance in the degradation of methyl blue (MB). To the best of our knowledge, this is the first study of creating diverse yet elaborate 3D hierarchical $SrTiO_3$ architectures simply by a one-pot reaction.

## 2. Experimental section

### 2.1 Fabrication of garden-like $SrTiO_3$ hierarchical structures

Hierarchically structured garden-like $SrTiO_3$ grown on transparent conducting substrates was formed by a combination of chemical bath synthesis and subsequent hydrothermal treatment. In a typical synthesis, 20 mL 0.025 M $Zn(NO_3)_2$ (Sigma-Aldrich, purity ≥98.0%) aqueous solution with 0.0125 M hexamethylenetetramine (HMTA, Sigma-Aldrich, purity ≥99.0%) was prepared, having a pH of 11.00 adjusted by adding ammonia. A fluorine-doped tin oxide (FTO) substrate (F:$SnO_2$, 2 cm × 2 cm, 14 Ω square$^{-1}$; Pilkington Glass, USA) ultrasonically cleaned for 30 min in a mixed solution of acetone and ethanol with a volume ratio of 1 : 1, followed by rinsing with deionized water for 15 min was placed in a sealed glass bottle containing the $Zn(NO_3)_2$ aqueous solution prepared above with its conducting side facing up. The chemical bath reaction was performed at 85 °C for 4 h in an oven. Subsequently, the FTO substrate was taken out, rinsed extensively with deionized water, and then immersed in another aqueous solution with 0.1 M $(NH_4)_2TiF_6$ (Sigma-Aldrich, purity ≥99.99%) and 0.1 M $H_3BO_3$ (Sigma-Aldrich, purity ≥99.5%) at 25 °C for 2 h, followed by deionized water washing. Subsequently, a hydrothermal treatment was carried out in an aqueous solution containing 0.1 M $(CH_3COO)_2Sr$ (Sigma-Aldrich, purity ≥97.0%) at pH = 13.00 (measured using a pH meter) adjusted by adding 1 M NaOH solution at 180 °C for 24 h. The product was rinsed with dilute HCl solution to remove some existing impurities (*e.g.*, unreacted ZnO). The effects of hydrothermal growth conditions, including the growth time (from 3 h to 40 h), temperature (from 150–200 °C), initial concentrations of $(CH_3COO)_2Sr$, and acidity on the resulting hierarchical structures were systematically investigated. Similarly, $BaTiO_3$ films were obtained by hydrothermal synthesis in 0.05 M $(CH_3COO)_2Ba$ (Sigma-Aldrich, purity ≥99.0%) solution (pH = 13.50) at 200 °C, and $CaTiO_3$ films were prepared hydrothermally in 0.05 M $(CH_3COO)_2Ca$ (Sigma-Aldrich, purity ≥99.0%) solution (pH = 13.00) at 180 °C, while $Pb_2Ti_2O_6$ films were synthesized hydrothermally in 0.05 M $(CH_3COO)_2Pb$ (Sigma-Aldrich, purity ≥99.0%) solution (pH = 7.00) at 200 °C, followed by annealing at 600 °C to transform them into $PbTiO_3$.

### 2.2 Photocatalytic degradation of MB molecules

The photocatalytic activity of samples was evaluated by the degradation of methyl blue (MB) dye. The photocatalytic experiments were conducted in a quartz glass reactor. The reactor was equipped with a water jacket to control the reaction temperature. A 200 W high-pressure mercury lamp (GCQ200, Shanghai Jiguang Special Lighting Electrical Appliance Factory) emitting at a wavelength of 365 nm was employed as the UV light source. All experiments were performed under continuous stirring, using 30 mL of 10 mg $L^{-1}$ MB aqueous solution, and air was bubbled through a gas disperser into the reactor. The change of MB concentration with the degradation time was analyzed using a UV-vis spectrophotometer (Unico UV-2102 PC) at a wavelength of 664 nm.[21]

### 2.3 Characterization

The morphology and lattice structures of samples were examined by field emission scanning electron microscopy (FESEM; FEI Quanta 250, operating at 10 kV in high vacuum) and transmission electron microscopy (TEM; JEOL 2100, operating at 200 kV). A SEM equipped with an energy dispersive X-ray spectrometer (EDS, FEI Quanta 250, operating at 10 kV in high vacuum) was used to analyze the composition of the nanostructures. The phase identification of the materials was conducted by X-ray diffraction (XRD; SCINTAG XDS-2000, Cu Kα radiation; operating at a scan rate of 0.04° $s^{-1}$ and a step size of 0.02° in 2$\theta$). The light absorption of the films was measured by UV-visible spectroscopy (Varian; UV-vis-NIR spectrophotometer, Cary 5000). The Raman spectrum was recorded on a Renishaw Raman microspectrometer system 2000 equipped with a He–Ne laser (632.8 nm). The laser power was 5.6 mW on a sample with a light spot of diameter about 1 mm. Room-temperature photoluminescence (PL) was recorded using a fluorescence spectrophotometer (Hitachi High-Tech, F-7000) equipped with a xenon lamp as an excitation source (excitation at 325 nm).

## 3. Results and discussion

Fig. 1 shows the SEM images and XRD patterns of as-prepared products. As indicated in Fig. 1a, flower-like ZnO structures were formed *via* a chemical bath procedure in the basic solution (pH = 11.00) containing 0.025 M $Zn(NO_3)_2$ and 0.0125 M HMTA at 85 °C for 4 h. These well-defined ZnO flowers comprising several tapering sword-like petals with a length of approximately 2 μm and an average diameter of about 400 nm (inset in

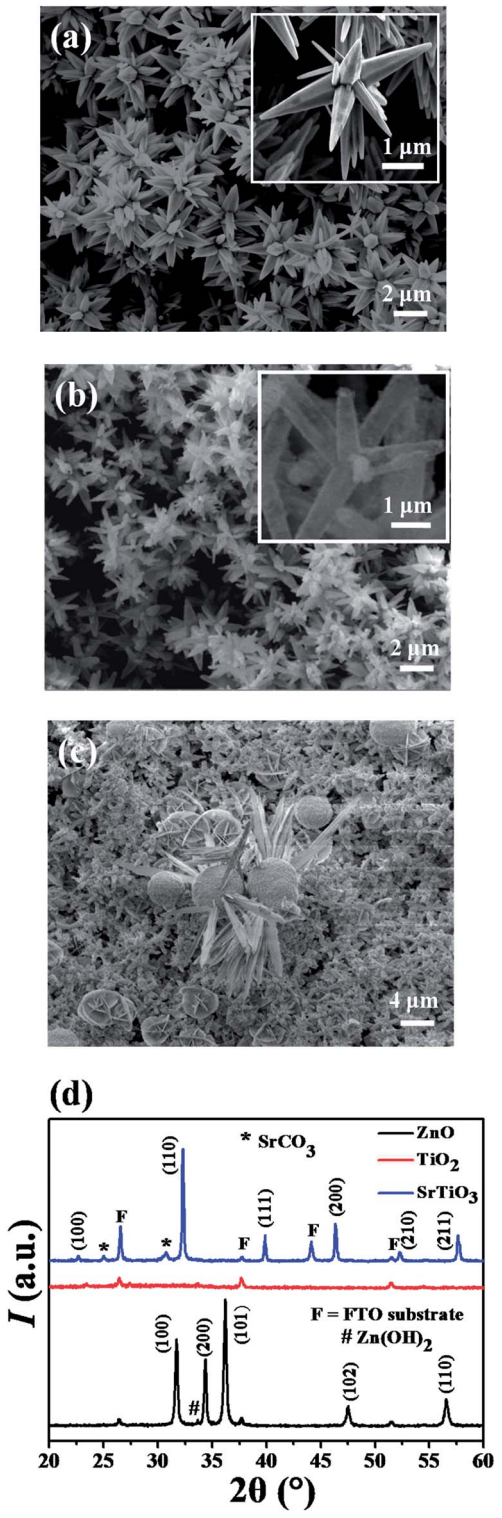


Fig. 1 SEM images of (a) ZnO flowers prepared in aqueous solution (pH = 11.00) containing 0.025 M $Zn(NO_3)_2$ and 0.0125 M HMTA at 90 °C for 4 h (the close-up of one ZnO flower is shown as the inset); (b) $TiO_2$ flowers produced by converting ZnO flowers in aqueous solution containing 0.1 M $(NH_4)_2TiF_6$ and 0.1 M $H_3BO_3$ at 25 °C for 2 h (the close-up of one $TiO_2$ flower is shown as the inset); and (c) $SrTiO_3$ garden created by hydrothermally treating $TiO_2$ flowers in aqueous solution (pH = 13.00) containing 0.1 M $(CH_3COO)_2Sr$ at 180 °C for 24 h. (d) XRD patterns of ZnO flowers, $TiO_2$ flowers and $SrTiO_3$ garden.

Fig. 1a) were used as templates and converted into $TiO_2$ flowers (Fig. 1b) after a 2 h-immersion in the aqueous solution containing 0.1 M $(NH_4)_2TiF_6$ and 0.1 M $H_3BO_3$ at 25 °C. The $TiO_2$ flower almost retained the structure of ZnO templates (inset in Fig. 1b). The $TiO_2$ petals appeared to be translucent hollow rods as reported in the literature[25] and had a rough surface (inset in Fig. 1b), which is distinctly different from the smooth surface of solid rod-shaped ZnO petals (inset in Fig. 1a). Subsequently, a hydrothermal treatment was performed to transform $TiO_2$ into hierarchical $SrTiO_3$ (Fig. 1c) in a basic (pH = 13.00) 0.1 M $(CH_3COO)_2Sr$ solution at 180 °C for 24 h. Interestingly, different $SrTiO_3$ architectures emerged on the FTO substrate (Fig. 1c and 2a), resembling a garden growing several plants, including the original flower-shaped structures composed of several nanorods (*i.e.*, sword-shaped petals; Fig. 2b) and new flowers made of many nanosheets (*i.e.*, sheet-shaped petals; Fig. 2c). Fig. 1d displays XRD patterns of the above-mentioned three products, in which the typical peaks were well-indexed to the standard hexagonal (wurtzite) structure (JCPDS no. 36-1451) for the ZnO film with a minor $Zn(OH)_2$ phase. The amorphous structure was, however, present in the $TiO_2$ film. The final product can be assigned to cubic $SrTiO_3$ (JCPDS no. 73-0661), which has an excellent crystalline nature, suggesting the successful transformation of $TiO_2$ into $SrTiO_3$. We note that there is a small

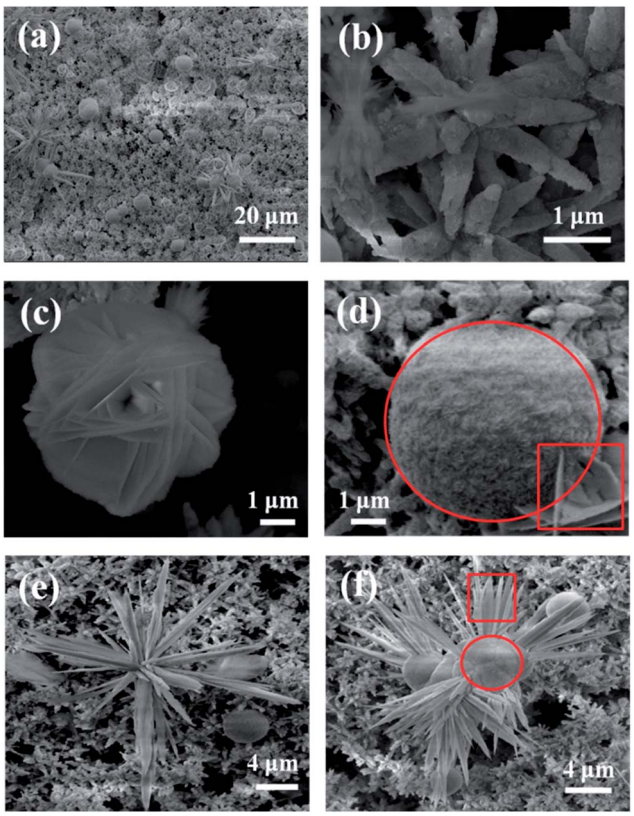


Fig. 2 SEM images of (a) a full top view of a $SrTiO_3$ garden, (b) $SrTiO_3$ flowers composed of hollow nanorods, (c) $SrTiO_3$ flowers assembled with nanosheets, (d) $SrTiO_3$ bouquet constructed with nanoflakes (see Fig. S2a† for a better view where nanoflakes are clearly evident), (e) $SrTiO_3$ grass containing long blades, and (f) hierarchically structured $SrTiO_3$ showing the coexistence of bouquet and grass.

quantity of $SrCO_3$ impurity in the product. Moreover, the EDS analysis further showed that only Zn and O elements in the ZnO template had an atomic ratio of Zn : O = 1 : 1 (Fig. S1a and S1d†); for $TiO_2$, in addition to Ti and O elements, a little of residual Zn from the ZnO template and a little of F adsorbing from the $(NH_4)_2TiF_6$ solution used for converting ZnO into $TiO_2$ were identified (Fig. S1b and S1d†); while in the case of $SrTiO_3$ structure, the atomic ratio of Sr : Ti : O was approximately 1 : 1 : 3, corresponding well to the molecular formula of strontium titanate (Fig. S1c and S1d†).

The detailed features of the $SrTiO_3$ garden are shown in Fig. 2 (SEM images) and Fig. 3 (TEM images). A full view of the garden is shown in Fig. 2a, indicating the coexistence of various structures in the garden. Fig. 2b presents the original flower composed of several nanorods with a diameter of the nanorod in the range of 300–500 nm and a length within 1–2 μm. However, these rod-shaped petals had a considerably rough surface (Fig. 2b) in comparison to the translucent hollow $TiO_2$ nanorods (inset in Fig. 1b). The mesoporous $SrTiO_3$ nanorod was hollow as evidenced by TEM imaging (Fig. 3a), where the center of the nanorod appeared relatively bright. In addition, another flower-like structure with a diameter of approximately 5 μm, assembled by many thin nanosheets as petals, was also developed (Fig. 2c). These nanosheets with a width in the range of 2–3 μm and a wall thickness of about 20 nm connected with each other to form a network resembling a flower (Fig. 2c). More interestingly, a uniformly shaped bouquet-like structure with a size ranging from 3–5 μm is seen in Fig. 2d. Further scrutiny of the $SrTiO_3$ bouquet revealed that such a 3D superstructure was constructed from dozens of squeezed and interacted flake-like petals of about 400 nm in width and 15 nm in wall thickness (Fig. S2a†). Furthermore, a grass-like structure composed of long blade-like building blocks emanating radially from a core with a length in the range of 4–8 μm and a width of 300 nm was synchronously grown (Fig. 2e). Noticeably, two different structures can emerge at the same time during the growth, for example, some long blade-like structures (marked with a red square in Fig. 2f) can intercalate into the bouquet-like structure (red circle in Fig. 2f), while some larger sheet-shaped petals (red square in Fig. 2d) implanted into the bouquet-like structure that was made of numerous smaller flake-shaped petals (red circle in Fig. 2d). Fig. 3a–d display the TEM images of the fragments of four representative building blocks, that is, a hollow nanorod (Fig. 3a, corresponding to Fig. 2b), several nanosheets (Fig. 3b, corresponding to Fig. 2c), a part of bouquet (Fig. 3c, corresponding to Fig. 2d) and a nanoblade (Fig. 3d, corresponding to Fig. 2e), respectively. The corresponding high resolution TEM (HRTEM) images of the four building blocks are shown in Fig. 3a′–d′. All of them had the same fringe spacing of approximately 0.275 nm. This corresponds to the (110) lattice spacing of the cubic phase of $SrTiO_3$, in accordance with the XRD measurement (Fig. 1d).

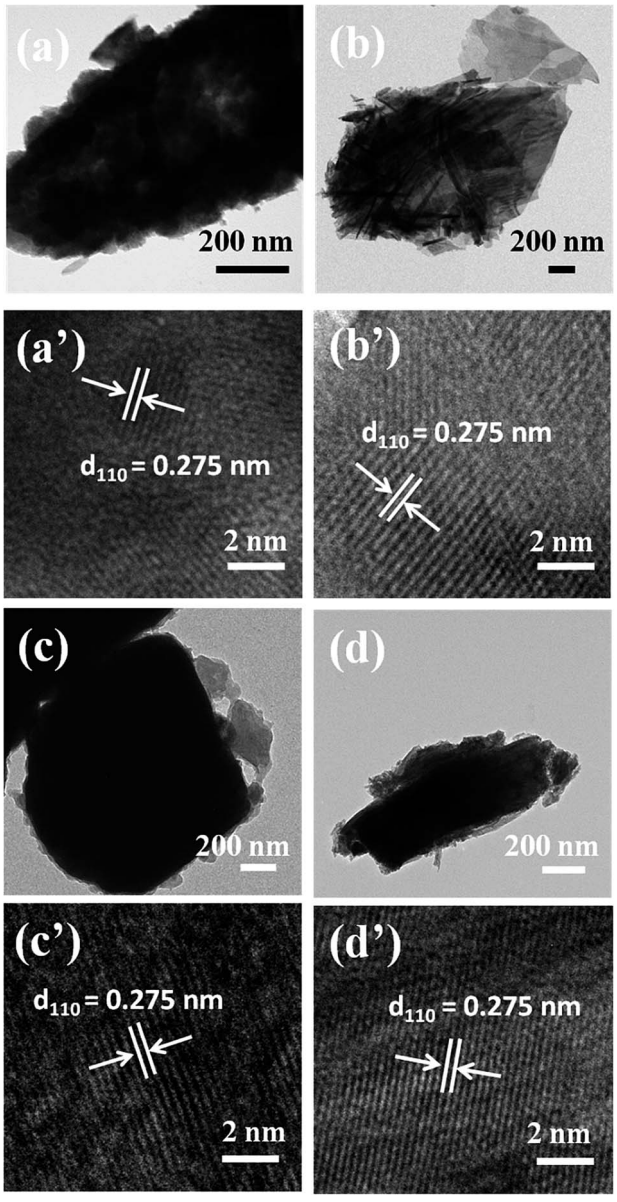


Fig. 3 TEM images of (a) a $SrTiO_3$ hollow nanorod; (b) several $SrTiO_3$ nanosheets; (c) part of the $SrTiO_3$ bouquet; (d) $SrTiO_3$ blade fragment. (a′–d′) HRTEM images, corresponding to TEM images in (a–d).

To further scrutinize the growth process of hierarchical architectures, the time-dependent evolution study and control experiments were performed and the resulting samples were examined by SEM and XRD. The typical SEM images of the samples obtained at different hydrothermal reaction times are shown in Fig. 4a–e. As evidenced in Fig. 4a, the sample obtained after 3 h only contained flower-like structures converted from $TiO_2$ without any other visible superstructures; however, the XRD measurement (Fig. 4f) revealed that these flowers were cubic $SrTiO_3$, suggesting the rapid transformation of amorphous $TiO_2$ into crystal $SrTiO_3$. As the hydrothermal reaction time increased to 6 h, some scattered bud-like protuberances (red circle in Fig. 4b) for bouquets were created and situated on the flower surface (Fig. 4b). Quite interestingly, the sheet-like building blocks (red circle in Fig. 4c) for the new flower-like structure (Fig. 2c) emerged as the reaction progressed (Fig. 4c). The prolonged reaction for 24 h yielded dense and ripen superstructures comprising diverse morphologies (Fig. 2a and 4d) due to the crystal growth. However, when the growth time

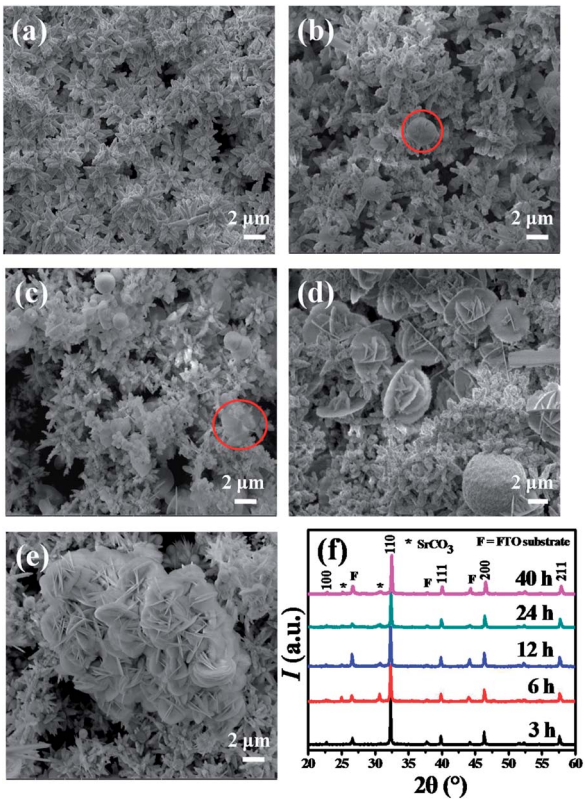


Fig. 4 SEM images of $SrTiO_3$ gardens produced by hydrothermal treatment for (a) 3 h, (b) 6 h, (c) 12 h, (d) 24 h, and (e) 40 h. (f) The corresponding XRD pattern of $SrTiO_3$ gardens prepared at different times.

was extended up to 40 h, several flowers were aggregated together, forming a bulky wreath-like morphology. In addition, Fig. S3† shows the photoluminescence (PL) emission of $SrTiO_3$ samples, which can be characterized by a typical multi-phonon process, namely, a system where the relaxation occurs *via* several routes, involving the participation of numerous states within the bandgap of the material due to intrinsic defects of the material.[10] The intensity of PL decreased with an increase in hydrothermal time, suggesting the gradually reduced recombination between electrons and holes trapped in the intermediate states to the band gap of $SrTiO_3$ samples.[26] Remarkably, the corresponding XRD (Fig. 4f) and PL (Fig. S3†) results implied that the appearance of this luxuriant garden may probably be ascribed to the transformation of unstable structures (*i.e.*, original flowers in Fig. 2b) into stable structures with reduced defects (*i.e.*, sheet-shaped flowers in Fig. 2c). These flower-like structures undergo the dissolution–recrystallization process, namely, the well-known Ostwald ripening process,[27,28] as will be discussed in more detail later.

In addition, the effects of the variation of hydrothermal conditions, including temperature, precursor concentration and pH, on the formation of hierarchical architectures were also explored. First, hydrothermal synthesis at lower temperature (180 °C) was found to only yield some rounded nanosheets with a width of about 6 μm and a wall thickness of 20 nm (Fig. S4a and S4b†), which loosely interacted with their adjacent nanosheets. In contrast, higher temperature synthesis (200 °C) introduced an increased reaction rate, thus leading to the complete transformation of original flowers into small but dense and irregular nanosheets of about 3 μm wide, which are randomly connected with their neighbors (Fig. S4c and S4d†). Subsequently, the study of the precursor concentration effect showed that a lower concentration of $(CH_3COO)_2Sr$ (0.05 M) resulted in the formation of a small quantity of rounded nanosheets with 3 μm in size (Fig. S5a and S5b†), while a higher concentration (0.2 M) resulted in many bougainvillea-like architectures composed of 2 μm wide fine sheet-shaped petals (Fig. S5c and S5d†). Finally, it was found that $OH^-$ played an important role in the generation of $SrTiO_3$ since it was impossible to obtain any crystalline $SrTiO_3$ when the pH was lower than 12.00 (Fig. S6a and S6b†). On the other hand, when the pH was increased up to 13.50, fine bundles composed of gracile nanowhiskers and small bud-like structures were apparently obtained (Fig. S6c and S6d†).

Due to their unique dielectric, piezoelectric, and ferroelectric properties,[5,16,17] in addition to $SrTiO_3$, other perovskite structures, such as $BaTiO_3$, $CaTiO_3$, and $PbTiO_3$ have also been intensively investigated. However, we note that many reported preparative routes are only capable of synthesizing one or two kinds of perovskites. In the present study, the synthesis of perovskite $MTiO_3$ (M = Ba, Ca, and Pb) was carried out by adjusting the reaction parameters used in the similar hydrothermal reaction. Under optimized conditions, the creation of well-defined superstructures can be readily realized for these three perovskite structures, that is, dendritic $BaTiO_3$ (Fig. 5a and 5b), nest-like $CaTiO_3$ (Fig. 6a), and plate-like pyrochlore $Pb_2Ti_2O_6$ (Fig. 6b) were observed. The XRD measurement revealed that $BaTiO_3$ had high crystallinity (Fig. 5c, JCPDS no. 83-1880). Moreover, Fig. 5d shows the Raman spectrum of the $BaTiO_3$ sample where the Raman peaks located at 186, 261 and 509 $cm^{-1}$ are related to the transverse optical (TO) modes of A1 symmetry, the peak at 304 $cm^{-1}$ is assigned to the B1 mode, and the peak at 719 $cm^{-1}$ corresponds to the highest frequency longitudinal optical mode (LO) with A1 symmetry. The existence of the Raman peak at 304 $cm^{-1}$ suggests the asymmetry within the $TiO_6$ octahedra of $BaTiO_3$ on a local scale, indicating the presence of the tetragonal $BaTiO_3$ phase.[29,30] However, for $CaTiO_3$, the XRD pattern showed that the as-prepared product can be indexed to an orthorhombic lattice (Fig. 6c; JCPDS no. 82-0229).[17] Quite interestingly, cubic pyrochlore $Pb_2Ti_2O_6$ (Fig. 6d; JCPDS no. 26-0142) was formed,[23] which is often observed as an intermediate phase during the preparation of the perovskite $PbTiO_3$ material. It is difficult to obtain the single-phase of $Pb_2Ti_2O_6$ because of the close stoichiometry to perovskite (Pb : Ti : O = 1 : 1 : 3) and metastable nature of $Pb_2Ti_2O_6$ at high temperature.[23] However, under hydrothermal conditions, well-crystallized cubic pyrochlore $Pb_2Ti_2O_6$ remained rather stable although a trace of impurities existed (Fig. 6d, additional peaks in the XRD pattern were from impurities, *e.g.*, $Pb_3O_2CO_3$ and $Ti_9O_7$). After thermal annealing at 600 °C for 2 h, cubic pyrochlore $Pb_2Ti_2O_6$ was transferred into cubic $PbTiO_3$ (Fig. S7a,† JCPDS no. 40-0099). Notably, this

 

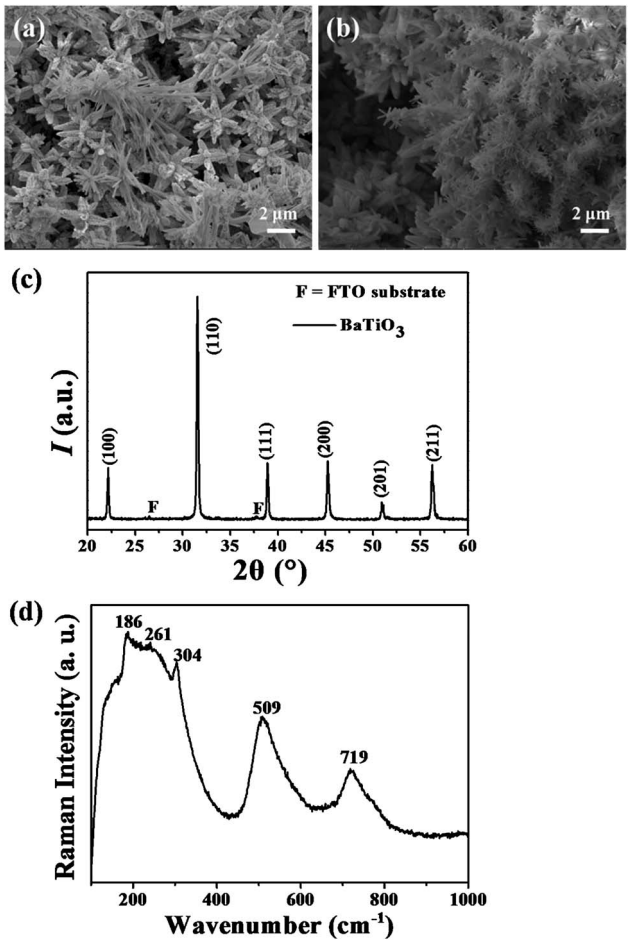


Fig. 5 SEM images of dendritic $BaTiO_3$ hydrothermally prepared in the 0.05 M $(CH_3COO)_2Ba$ solution (pH = 13.50) at 200 °C for (a) 12 h, and (b) 24 h. (c) XRD pattern and (d) the Raman spectrum of the sample in (b).

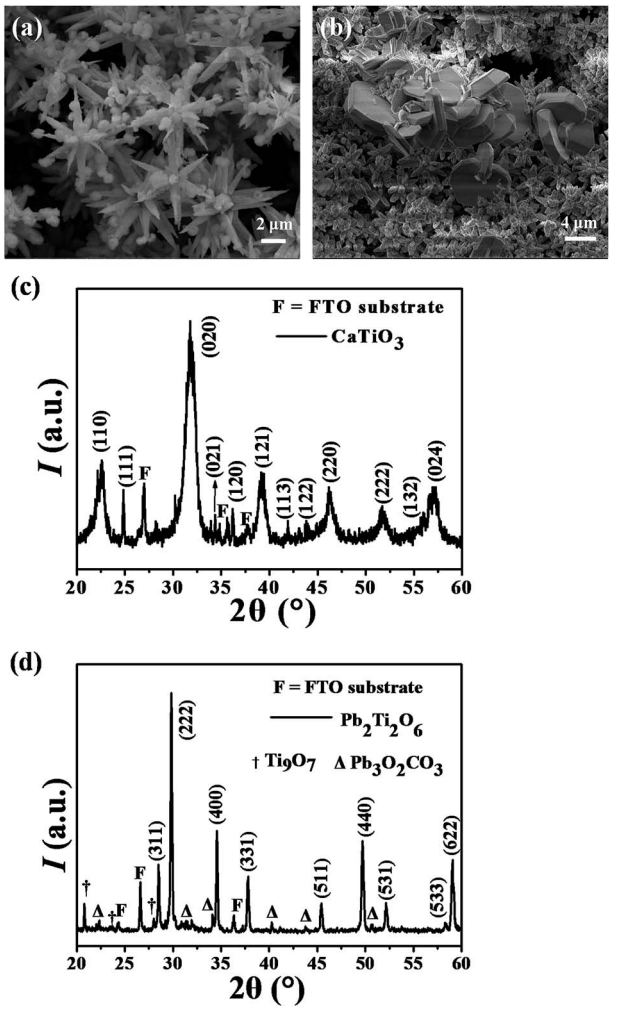


Fig. 6 SEM images of (a) $CaTiO_3$ hydrothermally prepared in 0.05 M $(CH_3COO)_2Ca$ solution at pH = 13.00 at 180 °C for 24 h, and (b) $Pb_2Ti_2O_6$ hydrothermally synthesized in 0.05 M $(CH_3COO)_2Pb$ solution at pH = 7.00 at 200 °C for 24 h. (c and d) XRD patterns of (c) $CaTiO_3$ and (d) $Pb_2Ti_2O_6$, respectively.

observation is totally different from a recent report where cubic pyrochlore $Pb_2Ti_2O_6$ was converted into the tetragonal phase by calcination,[31] partially due to the morphological difference between the present study and that reported in the literature as the change of crystal size can affect both lattice structure and polarization.[32] In addition, Fig. S7b† shows the profile of photoluminescence (PL) emission of $PbTiO_3$, which implies that the intrinsic defects of $PbTiO_3$ were largely reduced *via* the thermal transformation as reflected by the reduced intensity of PL spectra.

We now turn our attention to elucidate the possible growth mechanism of $MTiO_3$ (M = Sr, Ba, Ca and Pb) with various microstructures. As reported in the literature, solid ZnO nanorods can be readily converted into hollow $TiO_2$ nanorods *via* liquid-phase $TiO_2$ deposition and simultaneous ZnO dissolution by immersing ZnO nanorods in an aqueous solution consisting of $(NH_4)_2TiF_6$ and $H_3BO_3$.[25] This conversion facilitated the subsequent hydrothermal synthesis of perovskite structures. To date, there have been two possible mechanisms to account for the formation of $MTiO_3$ under hydrothermal conditions:[4,33] (1) heterogeneous nucleation by which *in situ* transformation of $TiO_2$ into $MTiO_3$ occurs due to inward diffusion of dissolved $M^{2+}$;[33] (2) homogeneous nucleation in which the dissolution–precipitation process takes place *via* the dissolution of some soluble $TiO_2$ as hydroxyl–titanium complexes (*i.e.*,$[Ti(OH)_6]^{2-}$) and subsequent precipitation of $MTiO_3$ crystals as a result of the reaction between $[Ti(OH)_6]^{2-}$ and $M^{2+}$, either homogeneously in solution or heterogeneously on $TiO_2$.[4] Depending on reaction conditions, both mechanisms may occur simultaneously or one dominates over the other.[8,27,28,34–36] On the basis of morphological features observed in the present study, we proposed that the formation of $MTiO_3$ superstructures may be governed by the dissolution and precipitation mechanism (*i.e.*, mechanism (2) as noted above), followed by the Ostwald ripening process of perovskite nanocrystals and self-organization of perovskite building blocks. The evolution process is illustrated in Scheme 1. At the first stage, in the basic solution titanium species (*i.e.*, $[Ti(OH)_6]^{2-}$) that dissolved from the surface of $TiO_2$ flowers (Scheme 1b) grown directly from the ZnO template (Scheme 1a) can react with abundant $M^{2+}$ to form

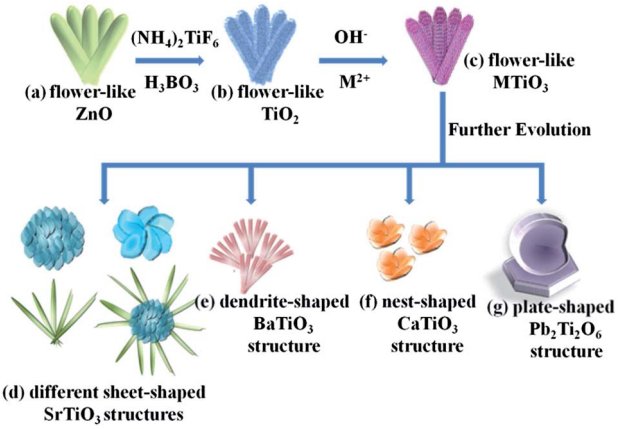


Scheme 1 Schematic illustration of the formation mechanism of $MTiO_3$ with various superstructures.

$MTiO_3$ nuclei predominantly on the $TiO_2$ surface; then the nuclei grow into small nanoparticles.[34] The dissolution of $TiO_2$ and precipitation of $MTiO_3$ occuring in the vicinity of the flower surfaces can be probably attributed to the rapid reaction between the as-formed $[Ti(OH)_6]^{2-}$ and $M^{2+}$ to yield $MTiO_3$ that nucleated on the surface of $TiO_2$ flowers.[34] As the reaction proceeds, the formed $MTiO_3$ nanoparticles are accumulated on the surface of $TiO_2$ flowers to produce a particulate layer. After complete consumption of the remaining $TiO_2$ precursor, mesoporous $MTiO_3$ flowers composed of hollow nanorods (Scheme 1c) are well replicated from $TiO_2$ flowers. Subsequently, new architectures grow at the expense of small and less crystalline particles. According to the well-known dissolution–recrystallization process (*i.e.*, Ostwald ripening process),[34,37] the reduction in surface energy drives the crystal growth and morphological evolution due to the difference in solubility between large particles and small particles. Finally, as the reaction continues under prolonged reaction time and high temperature, nanoparticles disappear due to the dissolution (*e.g.*, $CaTiO_3$ formed at 180 °C for 40 h (Fig. S2c†); $SrTiO_3$ prepared at 200 °C for 24 h (Fig. S4c and S4d†)). Notably, due to different crystal growth nature, different $MTiO_3$ structures have their preferred growth orientations, which accounts for diverse final structures,[27,28] including nanosheets for $SrTiO_3$ (Fig. S2a†), nanoneedles for $BaTiO_3$ (Fig. S2b†), nanoslices for $CaTiO_3$ (Fig. S2c†), and microplates for $Pb_2Ti_2O_6$ (Fig. S2d†). These structures interact with one another and self-organize into elaborate hierarchical superstructures (Schemes 1d–g). In particular, a garden-like $SrTiO_3$ structure was developed under the selected hydrothermal condition (*i.e.*, 0.1 M $(CH_3COO)_2Sr$ at pH = 13.00 at 180 °C for 24 h). Apparently, under this mild reaction condition, the $SrTiO_3$ crystal nucleus successfully evolved into various morphologies (Scheme 1d). However, under other experimental conditions (*i.e.*, low and high temperatures, low and high precursor concentrations), the crystal nucleus grew uniformly, and only one final structure was developed. Clearly, more theoretical and experimental studies are needed to elucidate this result, and will be investigated in future work.

Fig. S8a† shows the UV-vis absorption spectra of as-prepared $MTiO_3$ materials, from which the absorption coefficient can be calculated based on the Lambert–Beer law.[38]

$$I = I_o \exp(-\alpha t) \quad (1)$$

$$A = \log(I_o/I) \quad (2)$$

$$\alpha = 2.303\ A/t \quad (3)$$

where $I_o$ is the intensity of incident light, $I$ is the intensity of transmitted light, $A$ is the optical absorbance (Fig. S8a†), $\alpha$ is the absorption coefficient, and $t$ is the film thickness, respectively. Subsequently, the optical band gap energy $E_g$ can be analyzed by the Tauc formula:[39,40]

$$(\alpha h\nu)^{1/n} = \beta(h\nu - E_g) \quad (4)$$

$$h\nu = 1240/\lambda \quad (5)$$

where $n$ depends on the characteristics of the transition in a semiconductor, which is either 1/2 for a direct inter-band transition (*e.g.*, $PbTiO_3$) or 2 for an indirect inter-band transition (*e.g.*, ZnO, $TiO_2$, $BaTiO_3$, $SrTiO_3$ and $CaTiO_3$), $h\nu$ is the discrete photon energy, $\lambda$ is the wavelength and $\beta$ is the absorption constant, respectively.[10,19,41] Accordingly, the $E_g$ of as-prepared $MTiO_3$ materials can thus be determined from the plot of $(\alpha h\nu)^{1/n}$ *vs.* $h\nu$ by extrapolating the intercept of the tangent of plot to $(\alpha h\nu)^{1/n} = 0$ (Fig. S8b and S8c†), As shown in Fig. S8b,† the band gap energies $E_g$ are 3.14 eV for ZnO, 3.18 eV for amorphous $TiO_2$ after annealing at 450 °C for 2 h, 3.46 eV for $SrTiO_3$, 3.09 eV for $BaTiO_3$, 3.24 eV for $CaTiO_3$, and 3.12 eV for $PbTiO_3$, respectively, signifying that their photocatalytic activities exist under UV-light irradiation.

It is worth noting that $SrTiO_3$ has superior photocatalytic activity as the bottom of its conduction band (CB) is determined by the Ti 3d states, which is even more negative (*i.e.*, −1.4 V *vs.* SCE) (using SCE as the reference electrode) than that of anatase $TiO_2$ (*i.e.*, −1.2 V *vs.* SCE), suggesting that $SrTiO_3$ has a stronger reduction ability.[12,42,43] In the present study, the photocatalytic activity of these hierarchically structured $MTiO_3$ materials was evaluated through the photodegradation of methyl blue (MB) under UV light activation. The variations of dye concentration at the time interval of 30 min are shown in Fig. 7a. It is not surprising that 7% of MB was degradable after 120 min in the absence of a catalyst because of its self-degradation characteristics under UV light illumination. Enhanced photocatalytic performance was obtained in the presence of all as-prepared materials. The order of photocatalytic activity followed $SrTiO_3$ > ZnO > $TiO_2$ > $PbTiO_3$ > $BaTiO_3$ > $CaTiO_3$. Remarkably, $SrTiO_3$ led to 75% removal of MB after the 2 h photodegradation, showing the best photocatalytic performance among the six catalysts.

The photocatalytic decomposition of MB can be described by the Langmuir–Hinshelwood kinetic model. The first-order linear relationship can be expressed as $\ln(C_o/C) = kt$, where $C_o$ and $C$ are the initial concentration of MB dye and the concentration of MB at time $t$ (the irradiation time), and $k$ is the apparent first-order reaction constant.[11,24] As indicated in

 

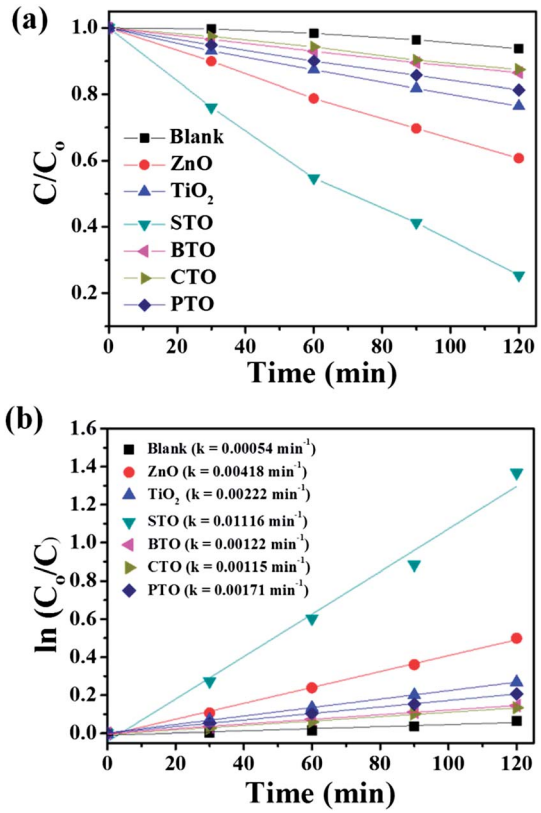


Fig. 7 Photocatalytic degradation rates of MB under UV light irradiation using different catalysts. (a) $C/C_0$ *vs.* *t*, and (b) $\ln(C_0/C)$ *vs.* *t*. STO, BTO, CTO, and PTO represent $SrTiO_3$, $BaTiO_3$, $CaTiO_3$, and $PbTiO_3$, respectively.

Fig. 7b, very low apparent reaction rate constants of $0.54 \times 10^{-3}$ $min^{-1}$, $1.15 \times 10^{-3}$ $min^{-1}$, $1.22 \times 10^{-3}$ $min^{-1}$, and $1.71 \times 10^{-3}$ $min^{-1}$ were obtained in the cases of the self-photolysis of MB, the photocatalysis by $CaTiO_3$, $BaTiO_3$ and $PbTiO_3$, respectively. ZnO and $TiO_2$ photocatalysis displayed relatively higher reaction rates of $4.54 \times 10^{-3}$ $min^{-1}$ and $2.22 \times 10^{-3}$ $min^{-1}$, respectively. In contrast, $SrTiO_3$ exhibited the highest reaction rate of $11.16 \times 10^{-3}$ $min^{-1}$, reflecting a 146% enhancement of photocatalytic efficiency when compared to that of ZnO. In addition, different $SrTiO_3$ structures prepared at different times were also examined. As demonstrated in Fig. S9a and S9b,† the reaction rate of MB decomposition increased from $1.07 \times 10^{-3}$ $min^{-1}$ to $7.00 \times 10^{-3}$ $min^{-1}$ and to $11.16 \times 10^{-3}$ $min^{-1}$ as hydrothermal growth time increased from 0 h (amorphous $TiO_2$ only) to 3 h and to 24 h, respectively. However, prolonged growth for 40 h led to reduced photocatalytic activity ($6.31 \times 10^{-3}$ $min^{-1}$). Obviously, this was possibly due to the crystal and morphological differences of samples, namely, amorphous $TiO_2$ flowers at 0 h (Fig. 1b), pure flower-like $SrTiO_3$ structure after 3 h (Fig. 4a), peculiar garden-like hierarchical architecture after 24 h (Fig. 2a and 4d), and large agglomerates after 40 h (Fig. 4e). It is well accepted that dark adsorption is a prerequisite for good photocatalytic activity. In general, 2D thin nanosheet structures have a large surface area and a good diffusion state, which substantially facilitate the dye loading.[44] Accordingly, Fig. S9c† reveals that after 1 h dark adsorption the order of adsorption capacity of $SrTiO_3$ samples followed $SrTiO_3$ (24 h) > $SrTiO_3$ (3 h) > $SrTiO_3$ (40 h) > $SrTiO_3$ (0 h; *i.e.*, pure $TiO_2$ flowers), which correlated well with the photocatalytic results. It is noteworthy that in comparison to other materials, $SrTiO_3$ still showed the best adsorption capacity, which may be considered as an additional major reason for its highest photocatalytic activity. Alternatively, the $SrTiO_3$ garden-like structure was partially built from layered structures (*i.e.*, hydrothermally treated for 24 h); and the layer- or sheet-like architectures have been proven to be more favorable for diffusion and separation of photoexcited charge carriers.[19,45] Due to their layer- or sheet-like configuration, only through very short distance the generated holes can easily diffuse to the sheet surface where they are subsequently captured by surrounding $H_2O$, $OH^-$ or $O_2$ to form oxygen species (*e.g.*, $OH^{\bullet}$) which then react with MB. Consequently, the recombination process of charge carriers is substantially reduced, and thus the excited electrons can also effectively diffuse to the surface of $SrTiO_3$ to degrade the MB molecules.[19] Taken together, $SrTiO_3$ with the garden-like superstructures prepared from 0.1 M $(CH_3COO)_2Sr$ at pH = 13.00 at 180 °C for 24 h yielded the best performance among other materials in the MB degradation in this work.

## 4. Conclusion

In summary, garden-like cubic $SrTiO_3$ superstructures were directly grown on transparent conducting substrates by a combination of chemical bath synthesis and hydrothermal treatment. This *in situ* growth approach rendered the formation of diverse yet elaborate superstructures in one sample. A comprehensive study on the effects of growth time, temperature, initial concentration of precursor, and acidity on the creation of diversified morphologies of $SrTiO_3$ was performed. Interestingly, this approach is general and can be utilized to produce other perovskite (*e.g.*, $BaTiO_3$ and $CaTiO_3$) and pyrochlore ($Pb_2Ti_2O_6$) structures. Remarkably, in this work the garden-like $SrTiO_3$ superstructures exhibited superior photocatalytic performance in photodegradation of MB dyes as compared to other semiconductor photocatalysts (*i.e.*, ZnO, $TiO_2$, $BaTiO_3$, $CaTiO_3$ and $PbTiO_3$), primarily due to their hierarchical architectures with enhanced diffusion and improved dye adsorption capacity.

## Acknowledgements

M.Y. gratefully acknowledges the financial support from the Chinese Scholarship Council. This work is supported by the National Natural Science Foundation of China (51072170, 21021002) and the National Basic Research Program of China (2012CB932900) (C.L.), and Minjiang Scholar Program and Georgia Institute of Technology (Z.L.)

## Notes and references

1 M. A. Peña and J. L. G. Fierro, *Chem. Rev.*, 2001, **101**, 1981–2018.

2 X. Pang, Y. He, B. Jiang, J. Iocozzia, L. Zhao, H. Guo, J. Liu, M. Akinc, N. Bowler, X. Tan and Z. Lin, *Nanoscale*, 2013, **5**, 8695–8702.
3 J. Wang, X. Pang, M. Akinc and Z. Lin, *J. Mater. Chem.*, 2010, **20**, 5945–5949.
4 D. R. Modeshia and R. I. Walton, *Chem. Soc. Rev.*, 2010, **39**, 4303–4325.
5 N. Bao, L. Shen, G. Srinivasan, K. Yanagisawa and A. Gupta, *J. Phys. Chem. C*, 2008, **112**, 8634–8642.
6 V. R. Calderone, A. Testino, M. T. Buscaglia, M. Bassoli, C. Bottino, M. Viviani, V. Buscaglia and P. Nanni, *Chem. Mater.*, 2006, **18**, 1627–1633.
7 O. G. Vendik, E. K. Hollmann, A. B. Kozyrev and A. M. Prudan, *J. Supercond.*, 1999, **12**, 325–338.
8 D. Wang, J. Ye, T. Kako and T. Kimura, *J. Phys. Chem. B*, 2006, **110**, 15824–15830.
9 R. Konta, T. Ishii, H. Kato and A. Kudo, *J. Phys. Chem. B*, 2004, **108**, 8992–8995.
10 J. Ng, S. Xu, X. Zhang, H. Y. Yang and D. D. Sun, *Adv. Funct. Mater.*, 2010, **20**, 4287–4294.
11 X. Zhang, K. Huo, L. Hu, Z. Wu and P. K. Chu, *J. Am. Ceram. Soc.*, 2010, **93**, 2771–2778.
12 Z. Zheng, B. Huang, X. Qin, X. Zhang and Y. Dai, *J. Colloid Interface Sci.*, 2011, **358**, 68–72.
13 L. F. da Silva, W. Avansi Jr, J. Andres, C. Ribeiro, M. L. Moreira, E. Longo and V. R. Mastelaro, *Phys. Chem. Chem. Phys.*, 2013, **15**, 12386–12393.
14 D. Arney, T. Watkins and P. A. Maggard, *J. Am. Ceram. Soc.*, 2011, **94**, 1483–1489.
15 B. Im, H. Jun, K. H. Lee, S.-H. Lee, I. K. Yang, Y. H. Jeong and J. S. Lee, *Chem. Mater.*, 2010, **22**, 4806–4813.
16 Z. Ren, G. Xu, Y. Liu, X. Wei, Y. Zhu, X. Zhang, G. Lv, Y. Wang, Y. Zeng, P. Du, W. Weng, G. Shen, J. Z. Jiang and G. Han, *J. Am. Chem. Soc.*, 2010, **132**, 5572–5573.
17 X. Yang, J. Fu, C. Jin, J. Chen, C. Liang, M. Wu and W. Zhou, *J. Am. Chem. Soc.*, 2010, **132**, 14279–14287.
18 M. Alfredsson, F. Corà, D. P. Dobson, J. Davy, J. P. Brodholt, S. C. Parker and G. D. Price, *Surf. Sci.*, 2007, **601**, 4793–4800.
19 T.-D. Nguyen-Phan, E. J. Kim, S. H. Hahn, W.-J. Kim and E. W. Shin, *J. Colloid Interface Sci.*, 2011, **356**, 138–144.
20 G. Wang, R. Sæterli, P. M. Rørvik, A. T. Van Helvoort, R. Holmestad, T. Grande and M.-A. Einarsrud, *Chem. Mater.*, 2007, **19**, 2213–2221.
21 C. Wang, M. Wang, K. Xie, Q. Wu, L. Sun, Z. Lin and C. Lin, *Nanotechnology*, 2011, **22**, 305607.
22 Y. Wang, G. Xu, L. Yang, Z. Ren, X. Wei, W. Weng, P. Du, G. Shen and G. Han, *J. Cryst. Growth*, 2009, **311**, 2519–2523.
23 G. Xu, W. He, Y. Zhao, Y. Liu, Z. Ren, G. Shen and G. Han, *CrystEngComm*, 2011, **13**, 1498–1503.
24 X. Wei, G. Xu, Z. Ren, C. Xu, W. Weng, G. Shen and G. Han, *J. Am. Ceram. Soc.*, 2010, **93**, 1297–1305.
25 C. Xu, P. H. Shin, L. Cao, J. Wu and D. Gao, *Chem. Mater.*, 2009, **22**, 143–148.
26 A. Souza, G. Santos, B. Barra, W. Macedo Jr, S. Teixeira, C. Santos, A. Senos, L. Amaral and E. Longo, *Cryst. Growth Des.*, 2012, **12**, 5671–5679.
27 W. Dong, B. Li, Y. Li, X. Wang, L. An, C. Li, B. Chen, G. Wang and Z. Shi, *J. Phys. Chem. C*, 2011, **115**, 3918–3925.
28 Y. Li, X. P. Gao, G. R. Li, G. L. Pan, T. Y. Yan and H. Y. Zhu, *J. Phys. Chem. C*, 2009, **113**, 4386–4394.
29 C. An, C. Liu, S. Wang and Y. Liu, *Mater. Res. Bull.*, 2008, **43**, 932–938.
30 Z. Deng, Y. Dai, W. Chen, X. Pei and J. Liao, *Nanoscale Res. Lett.*, 2010, **5**, 1217–1221.
31 Y. Wang, G. Xu, L. Yang, Z. Ren, X. Wei, W. Weng, P. Du, G. Shen and G. Han, *J. Alloys Compd.*, 2009, **481**, L27–L30.
32 B. A. Hernandez-Sanchez, K.-S. Chang, M. T. Scancella, J. L. Burris, S. Kohli, E. R. Fisher and P. K. Dorhout, *Chem. Mater.*, 2005, **17**, 5909–5919.
33 M. Ryu, T. Suzuki, K. Kobayashi, T. Sakashita and Y. Mizuno, *Jpn. J. Appl. Phys.*, 2010, **49**, 1101.
34 T. Cao, Y. Li, C. Wang, C. Shao and Y. Liu, *Langmuir*, 2011, **27**, 2946–2952.
35 S. Dudley, T. Kalem and M. Akinc, *J. Am. Ceram. Soc.*, 2006, **89**, 2434–2439.
36 K. Zagar, A. Recnik, P. M. Ajayan and M. Ceh, *Nanotechnology*, 2010, **21**, 375605.
37 U. A. Joshi and J. S. Lee, *Small*, 2005, **1**, 1172–1176.
38 B. Su and K. L. Choy, *J. Mater. Chem.*, 2000, **10**, 949–952.
39 M. F. Budiman, W. G. Hu, M. Igarashi, R. Tsukamoto, T. Isoda, K. M. Itoh, I. Yamashita, A. Murayama, Y. Okada and S. Samukawa, *Nanotechnology*, 2012, **23**, 065302.
40 J. Tauc, A. Menth and D. L. Wood, *Phys. Rev. Lett.*, 1970, **25**, 749–752.
41 H. Gu, Y. Hu, J. You, Z. Hu, Y. Yuan and T. Zhang, *J. Appl. Phys.*, 2007, **101**, 024319.
42 I. Hod, M. Shalom, Z. Tachan, S. Rühle and A. Zaban, *J. Phys. Chem. C*, 2010, **114**, 10015–10018.
43 S.-D. Mo, W. Y. Ching, M. F. Chisholm and G. Duscher, *Phys. Rev. B: Condens. Matter Mater. Phys.*, 1999, **60**, 2416–2424.
44 Y. H. Chen and Y. D. Chen, *J. Hazard. Mater.*, 2011, **185**, 168–173.
45 Z. Xing, B. Geng, X. Li, H. Jiang, C. Feng and T. Ge, *CrystEngComm*, 2011, **13**, 2137–2142.